High-resolution laser spectroscopy of $^{27-32}$Al

H. Heylen,[1,2,3,*] C. S. Devlin [4] W. Gins [2,5] M. L. Bissell,[6] K. Blaum [3] B. Cheal [4] L. Filippin,[7] R. F. Garcia Ruiz,[1,6,†]
M. Godefroid,[7] C. Gorges,[8] J. D. Holt [9,10] A. Kanellakopoulos,[2] S. Kaufmann,[8,11] Á. Koszorús,[2] K. König [8,‡]
S. Malbrunot-Ettenauer,[1] T. Miyagi,[9] R. Neugart,[3,11] G. Neyens [1,2] W. Nörtershäuser,[8] R. Sánchez [12] F. Sommer,[8]
L. V. Rodríguez,[3,13] L. Xie,[6] Z. Y. Xu,[2] X. F. Yang,[2,14] and D. T. Yordanov[13]

[1]*Experimental Physics Department, CERN, CH-1211 Geneva 23, Switzerland*
[2]*Instituut voor Kern- en Stralingsfysica, KU Leuven, 3001 Leuven, Belgium*
[3]*Max-Planck-Institut für Kernphysik, D-69117 Heidelberg, Germany*
[4]*Oliver Lodge Laboratory, Oxford Street, University of Liverpool, Liverpool, L69 7ZE, United Kingdom*
[5]*Department of Physics, University of Jyväskylä, PB 35 (YFL), 40014 Jyväskylä, Finland*
[6]*School of Physics and Astronomy, The University of Manchester, Manchester, M13 9PL, United Kingdom*
[7]*Spectroscopy, Quantum Chemistry and Atmospheric Remote Sensing (SQUARES), Université libre de Bruxelles, 1050 Brussels, Belgium*
[8]*Institut für Kernphysik, Technische Universität Darmstadt, 64289 Darmstadt, Germany*
[9]*TRIUMF, 4004 Wesbrook Mall, Vancouver, British Columbia, Canada V6T 2A3*
[10]*Department of Physics, McGill University, 3600 Rue University, Montréal, Canada QC H3A 2T8*
[11]*Institut für Kernchemie, Universität Mainz, 55128 Mainz, Germany*
[12]*GSI Helmholtzzentrum für Schwerionenforschung, 64291 Darmstadt, Germany*
[13]*Institut de Physique Nucléaire, CNRS-IN2P3, Université Paris-Sud, Université Paris-Saclay, 91406 Orsay, France*
[14]*School of Physics and State Key Laboratory of Nuclear Physics and Technology, Peking University, Beijing 100871, China*

Hyperfine spectra of $^{27-32}$Al ($Z = 13$) have been measured at the ISOLDE-CERN facility via collinear laser spectroscopy using the $3s^23p\ ^2P^o_{3/2} \rightarrow 3s^24s\ ^2S_{1/2}$ atomic transition. For the first time, mean-square charge radii of radioactive aluminum isotopes have been determined alongside the previously unknown magnetic dipole moment of ^{29}Al and electric quadrupole moments of ^{29,30}Al. A potentially reduced charge radius at $N = 19$ may suggest an effect of the $N = 20$ shell closure, which is visible in the Al chain, contrary to other isotopic chains in the *sd* shell. The experimental results are compared with theoretical calculations in the framework of the valence-space in-medium similarity renormalization group using multiple sets of two- and three-nucleon forces from chiral effective field theory. While the trend of experimental magnetic dipole and electric quadrupole moments is well reproduced, the absolute values are underestimated by theory, which is consistent with earlier studies. Moreover, both the scale and trend of the charge radii appear to be very sensitive to the chosen interaction.

I. INTRODUCTION

Laser spectroscopy performed at radioactive ion beam facilities is a powerful technique to study isotopes all across the chart of nuclei [1]. By measuring atomic (or ionic) hyperfine spectra, ground, and isomeric state spins, electromagnetic moments and differences in mean-square charge radii can be obtained in a nuclear-model-independent way. Since these observables probe different nuclear structure aspects, laser spectroscopic studies are ideal to systematically investigate the performance of state-of-the-art nuclear theories.

In the last few decades, tremendous progress has been made in solving the nuclear many-body problem from first principles. Chiral effective field theory [2,3] provides microscopic interactions rooted in QCD, the fundamental theory of the strong interaction, while novel methods to solve the many-body Schrödinger equation in medium- and heavy-mass nuclei have been developed. Combined with the advances in computing power, a rapidly growing number of nuclides can be described within such an *ab initio* framework [4]. Particularly, the valence-space in-medium similarity renormalization group (VS-IMSRG) method [5–8] has emerged as a versatile tool to study open-shell nuclei in the medium-mass region. Its scope now reaches up to the tin region [8–10] and recently also isotopes requiring multishell valence spaces, e.g., nuclei in islands of inversion, have become accessible

---

*hanne.heylen@cern.ch

†Present address: Massachusetts Institute of Technology, Cambridge, Massachusetts, USA.

‡Present address: National Superconducting Cyclotron Laboratory, Michigan State University, East Lansing, Michigan 48824, USA.
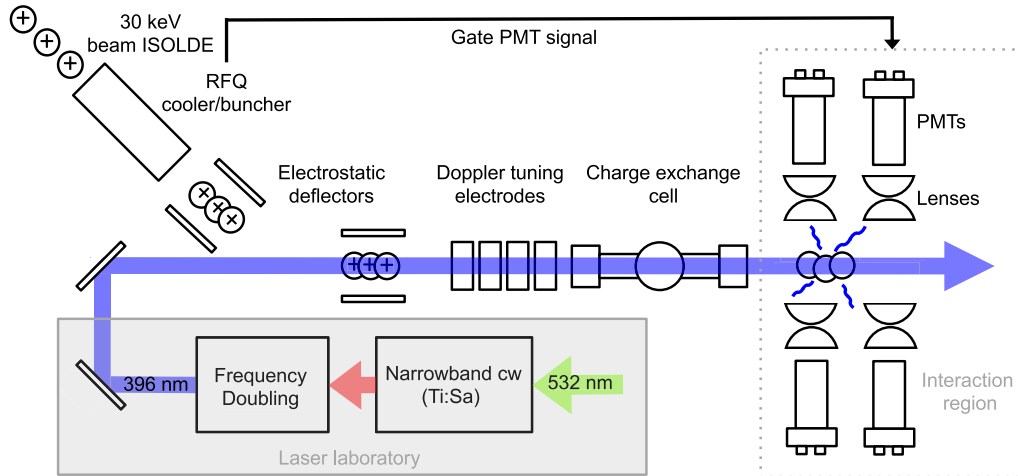
FIG. 1. Schematic depiction of the COLLAPS collinear laser spectroscopy setup at ISOLDE-CERN. More details can be found in the text.

[11]. Not limited to (near-)magic nuclei, the VS-IMSRG technique allows the exploration of the microscopic origins of global features such as the driplines [12], new magic numbers [13], and Gamow-Teller quenching [14], or local features along an isotopic chain, e.g., odd-even staggering in binding energies and radii [15] or the development of $E2$ strength [16,17]. These studies illustrate the importance of observables beyond binding energies to gain complementary insights in the validity of a theoretical approach. Nevertheless, a comprehensive investigation of a wide range of properties and isotopes using *ab initio* machinery has only just begun.

In this article, we focus on the magnetic dipole moments μ, electric quadrupole moments Q_s, and changes in mean-square charge radii, $\delta\langle r^2\rangle$, of the ground states of the aluminum isotopes $^{27-32}$Al ($Z = 13$). Because a proper treatment of correlations is important to describe the structure of midshell nuclei like Al, these isotopes are interesting candidates to gauge the performance of the latest advances in VS-IMSRG calculations.

Experimentally, the aluminum isotopic chain has been studied extensively in the past (see e.g., Refs. [18–24]) but the magnetic moment of ^{29}Al and quadrupole moments of ^{29,30}Al were not yet determined. Furthermore, the collinear laser spectroscopy experiment performed in this work provides for the first time charge radii of radioactive Al isotopes. In particular, the development of these radii towards the $N = 20$ shell closure is of interest.

II. EXPERIMENTAL DETAILS

The experiment has been performed at the COLLAPS collinear laser spectroscopy beam line [25] at ISOLDE-CERN [26]. A schematic of the setup can be seen in Fig. 1 and more details can be found in Refs. [25,27]. Neutral atoms of $^{27-32}$Al were produced by bombarding a uranium carbide target with 1.4-GeV protons from the PS booster. These isotopes were subsequently extracted from the target, ionized by ISOLDE's resonance ionization laser ion source (RILIS) [28], accelerated to 30 keV, and mass separated. Afterwards, the ion beam passed through ISCOOL [29], a He-buffer-gas-

filled radiofrequency quadrupole (RFQ) cooler and buncher, where the ions were accumulated for approximately 50 ms and released in time bunches of a few μs. These ion bunches were then guided to the COLLAPS beamline where they were spatially overlapped with a copropagating laser beam. Before neutralising the singly charged ions to neutral atoms in an alkali-vapor-filled charge exchange cell, a Doppler-tuning voltage was applied to alter the ions' velocity and, hence, to scan the laser frequency in the reference frame of the atoms. Laser spectroscopy was performed on the $3s^23p$ $^2P^o_{3/2} \rightarrow$ $3s^24s$ $^2S_{1/2}$ atomic transition at 25 235.696 cm^{-1}. This transition was probed with around 2 mW of continuous-wave (cw) laser light generated by the frequency-doubled output of a titanium-sapphire ring laser. Laser-induced fluorescence was detected by a light collection system placed around the laser-atom interaction region. It consists of two rows of two photomultiplier tubes (PMTs), each associated with their corresponding imaging lens arrangement [27]. By gating the fluorescence signals on the passage of the atom bunches through the interaction region, background from continuously scattered laser light and PMT dark counts was suppressed by four orders of magnitude.

III. RESULTS

Experimental hyperfine spectra of $^{27-32}$Al are shown in Fig. 2. As illustrated for ^{27}Al in the first panel of the figure, each resonance corresponds to a transition between a hyperfine level of the $^2P^o_{3/2}$ lower and $^2S_{1/2}$ upper state level. The position of these resonances $\nu_{F,F'}$ is described by

$$\nu_{F,F'} = \nu_0 + \Delta\nu_{F'} - \Delta\nu_F,$$

where ν_0 is the unperturbed transition frequency between the fine-structure levels, referred to as the centroid frequency. $\Delta\nu_F$ and $\Delta\nu_{F'}$ are the frequency differences between the hyperfine states and their respective fine-structure levels. These depend on the hyperfine parameters A_J and B_J for each atomic
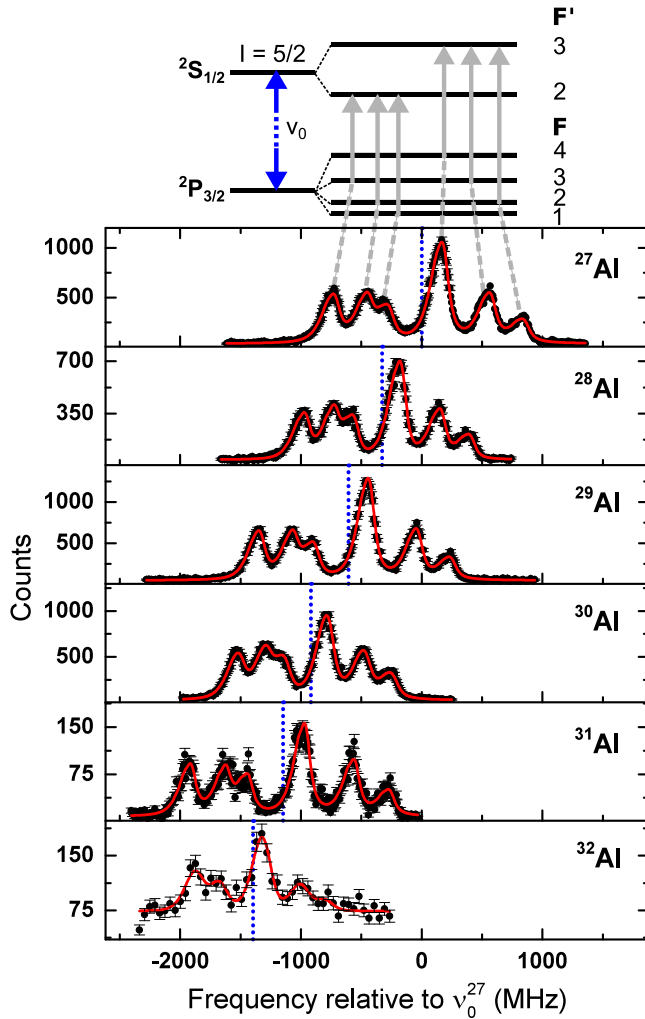
FIG. 2. Fluorescence counts as a function of frequency obtained for $^{27-32}$Al on the $3s^2 3p\ ^2P^o_{3/2} \rightarrow 3s^2 4s\ ^2S_{1/2}$ atomic transition. The red line represents the best fit. The centroid frequency ν_0 for each isotope is indicated with a vertical dashed line. On top of the figure, the hyperfine levels of an $I = 5/2$ nucleus like ^{27}Al are shown and the transitions probed using laser spectroscopy are indicated with gray arrows.

state J according to

$$\Delta \nu_F = A_J \frac{C}{2} + B_J \frac{3C(C+1) - I(I+1)J(J+1)}{8(2I-1)(2J-1)IJ}.$$

Here, I, J, and F ($F = I + J$) are the nuclear, atomic and total angular momenta, respectively, and $C = F(F+1) - I(I+1) - J(J+1)$.

The SATLAS analysis library [30] was used to fit the hyperfine structures using a χ^2-minimization procedure. In the fit, the centroid ν_0, and hyperfine parameters $A(P^o_{3/2})$ and $B(P^o_{3/2})$ were taken as free parameters while the ratio $A(S_{1/2})/A(P^o_{3/2}) = 4.5701$ was fixed to the value determined for the ^{27}Al reference isotope (obtained with an uncertainty of 0.0014). The intensities of the individual hyperfine peaks were left to vary freely in the fit. The asymmetric peak profiles, related to inelastic processes in the charge exchange cell

[27,31,32], were found to be best described by a Voigt profile including four satellite peaks at an empirically determined energy offset. This peak shape was applied to each of the hyperfine peaks. The relative intensities of these satellite peaks were constrained assuming Poisson's law.

For ^{27}Al, a statistically reasonable agreement with the known hyperfine parameters of the $P^o_{3/2}$ state was obtained [33–35], see Table I. The precision on the $A(S_{1/2}) = 431.11(9)$ MHz value of ^{27}Al deduced in this work was improved by more than two orders of magnitude as compared with the low-precision value in Ref. [36].

A. Nuclear moments

Table I shows the measured hyperfine $A(P^o_{3/2})$ and $B(P^o_{3/2})$ parameters of $^{27-32}$Al along with the magnetic dipole moments μ, and electric quadrupole moments Q_s extracted according to

$$\mu = \mu_{ref} \frac{AI}{A_{ref} I_{ref}}, \qquad Q_s = Q_{s,ref} \frac{B}{B_{ref}}.$$

Reference values for ^{27}Al were taken from Refs. [37,38] for the magnetic and quadrupole moment, respectively. The hyperfine anomaly was assumed to be negligible in the extraction of the magnetic moments. The present data provide for the first time an internally consistent set of Al moments determined with respect to a single reference isotope and measured in the same experimental conditions. This avoids potential discrepancies related to the applied shielding corrections or inconsistent electric field gradient calculations present when extracting magnetic and quadrupole moments from (β)-NMR experiments [39,40]. No systematic deviations between our moments and the available literature values were observed.

As seen from Table I, the previously unknown quadrupole moment of ^{30}Al ($I = 3$) and magnetic and quadrupole moment of ^{29}Al ($I = 5/2$) are similar to the moments of the Al isotopes with the same spin, suggesting a comparable nuclear structure. In general, it has been found that the aluminum ground states between $N = 14$ and $N = 19$ are well described within an sd picture [20].

B. Isotope shifts and mean-square charge radii

The measured isotope shifts, defined as $\delta \nu^{27,A} = \nu_0^A - \nu_0^{27}$, are shown in Table II. By alternating measurements of radioactive isotopes with those of the stable ^{27}Al reference, effects from drifts in experimental conditions largely cancel out. A systematic uncertainty on the deduced isotope shifts accounts for a 1.5×10^{-4} relative uncertainty on the beam energy.

From the measured isotope shifts, differences in mean-square charge radii, $\delta \langle r^2 \rangle^{27,A} = \langle r^2 \rangle^A - \langle r^2 \rangle^{27}$, can be extracted via [41]

$$\delta \nu^{27,A} = F \delta \langle r^2 \rangle^{27,A} + M \frac{m_A - m_{27}}{m_{27}(m_A + m_e)},$$

where m_A and m_{27} are the nuclear masses obtained by subtracting 13 electron masses from the atomic masses and m_e is the electron mass. The binding energy of the electrons has

TABLE I. Measured hyperfine $A(P_{3/2}^{\mathrm{o}})$ and $B(P_{3/2}^{\mathrm{o}})$ parameters and corresponding magnetic dipole moments μ and electric quadrupole moments Q_s for $^{27\text{–}32}$Al ground states. The hyperfine anomaly is expected to be small relative to the experimental precision and is neglected in the extraction of μ. The reference moments from ^{27}Al are taken from Refs. [37,38], which take into account recent atomic and molecular calculations of the hyperfine magnetic field and electric field gradients, necessary to extract μ and Q_s, respectively. Literature values for the other isotopes are reevaluated with respect to these reference values in Refs. [39,40]. References to the original experimental papers can be found in there.

A	N	I^π	$T_{1/2}$	$A(P_{3/2}^{\mathrm{o}})$ (MHz)	$B(P_{3/2}^{\mathrm{o}})$ (MHz)	μ_{expt} (μ_N)	μ_{lit} (μ_N)	$Q_{s,\mathrm{expt}}$ (fm^2)	$Q_{s,\mathrm{lit}}$ (fm^2)
27	14	$5/2^+$	stable	+94.33 (4)[a]	+18.1 (2)[a]	Reference	+3.64070 (2)	Reference	+14.66(10)
28	15	3^+	2.24 m	+70.07 (6)	+18.1 (8)	+3.245 (3)	3.241 (5)	+14.7 (7)	17.2 (12)
29	16	$5/2^+$	6.56 m	+94.97 (5)	+18.2 (6)	+3.665 (2)		+14.8 (5)	
30	17	3^+	3.62 s	+65.36 (7)	+14.9 (10)	+3.027 (4)	3.012 (7)	+12.1 (8)	
31	18	$5/2^+$	644 ms	+99.0 (3)	+19.3 (17)	+3.822 (11)	3.832 (5)	+15.6 (14)	13.40 (16)
32	19	1^+	33 ms	+124 (3)	+ 2 (6)	+1.92 (4)	1.953 (2)	+ 1(5)	2.5 (2)

[a]To be compared with the average of the literature values: $A(P_{3/2}^{\mathrm{o}}) = 94.25(4)$ MHz and $B(P_{3/2}^{\mathrm{o}}) = 18.8(3)$ MHz [33–35].

been neglected in this calculation. The atomic field shift and mass shift factors F and M, respectively, can be empirically calibrated via a King-plot procedure if the absolute charge radii of at least three isotopes are known from other techniques; see, for example, Ref. [42]. For chemical elements with a single stable isotope such as Al, only one absolute radius is known and one has to rely on atomic calculations instead. In these cases, a precise extraction of $\delta\langle r^2\rangle$ is often challenging since the mass shift, which dominates the isotope shift for relatively light elements like Al [43], is difficult to evaluate.

An in-depth investigation of the atomic factors for the $3s^2 3p\ ^2P_{3/2}^{\mathrm{o}} \rightarrow 3s^2 4s\ ^2S_{1/2}$ transition has previously been performed in the multiconfiguration Dirac-Hartree-Fock framework [44]. Two computational techniques (RATIP and RIS3) were adopted to study different electron correlation models: the core-valence + valence-valence (CV + VV) and core-valence + valence-valence + core-core correlations (CV + VV + CC), respectively. After analysis of the normal and specific contributions to the mass shift factor, it was found that the CV + VV model was the most reliable. Additionally, the effect of a common or separate optimization of the orbital basis sets for the lower and upper atomic states was explored.

TABLE II. Aluminum isotope shifts $\delta\nu^{27,A}$ measured in the $3s^2 3p\ ^2P_{3/2}^{\mathrm{o}} \rightarrow 3s^2 4s\ ^2S_{1/2}$ transition. The relative mean-square charge radii $\delta\langle r^2\rangle^{27,A}$ with respect to ^{27}Al are extracted from these isotope shifts using $M = -243$ GHz u and $F = 76.2$ MHz/fm^2. Systematic uncertainties due to a 1.5×10^{-4} relative uncertainty on the beam energy are indicated with square brackets, while the uncertainties on the $\delta\langle r^2\rangle^{27,A}$ arising from the atomic calculations of M and F are shown in curly parentheses.

A	N	$\delta\nu^{27,A}$ (MHz)	$\delta\langle r^2\rangle^{27,A}$ (fm^2)
27	14	0	0
28	15	−321.9 (8)[33]	+ 0.003 (10)[43]{72}
29	16	−610.7 (6)[64]	+0.141 (8)[84]{134}
30	17	−889.5 (12)[101]	+0.164 (15)[132]{196}
31	18	−1141.0 (12)[136]	+0.301 (16)[178]{250}
32	19	−1401 (7)[17]	+0.12 (9)[22]{31}

Although the CC effects were more balanced in the common optimization strategy, a separate optimization was necessary to properly treat orbital relaxation (i.e., to allow for an independent reorganization of the spectator electrons of the lower and upper states during the excitation process). Within the CV + VV correlation model, the separate optimization strategy was therefore preferred. Based on these considerations, in this work we selected the results of the CV + VV correlation model with separate optimization of basis states. The spread between the RIS3 ($F = 74$ MHz/fm^2 and $M = -239$ GHz u) and RATIP ($F = 78.4$ MHz/fm^2 and $M = -247$ GHz u) computational methods is a good indication of the uncertainty on the calculations. Note that, due to a different sign convention, the sign of M is opposite here as compared with Ref. [44].

Figure 3 shows the changes in mean-square charge radii of Al obtained this way alongside the experimental charge radii of chemical elements below and above Al. The good agreement between the Al radii and the regional systematics supports that the relevant physics is captured in the atomic calculations. For the extraction of the final $\delta\langle r^2\rangle$, see Table II, the average between the two computational methods was adopted: $M = -243 \pm 4$ GHz u and $F = 76.2 \pm 2.2$ MHz/fm^2. Here, $\pm$ refers to the range determined by the two methods, rather than to a 1σ uncertainty interval. This range established a systematic uncertainty on the extracted results. Additionally, the uncertainty on the isotope shift due to incomplete knowledge of the beam energy was propagated to the charge radii, shown by the shaded red band in Fig. 3. It is important to note that the systematic uncertainties, due to the beam energy as well as the atomic factors separately, act the same way and result in a slope of the charge radii which can change as a whole, but which does not affect the local details, like odd-even staggering and discontinuities.

Absolute mean-square charge radii $\langle r^2\rangle$ along the isotopic chain were extracted by combining our values for the differences in mean-square charge radii $\delta\langle r^2\rangle$ with the absolute mean-square charge radius of ^{27}Al. To obtain the latter, experimental data from muonic atom spectroscopy were combined with elastic electron scattering measurements according to the procedure laid out in Ref. [48]. We started from the Barrett equivalent radius $R_{k\alpha}^\mu = 3.9354(24)$ fm deduced from the $2p$-$1s$ transition energy in the muonic atom [48]. To extract
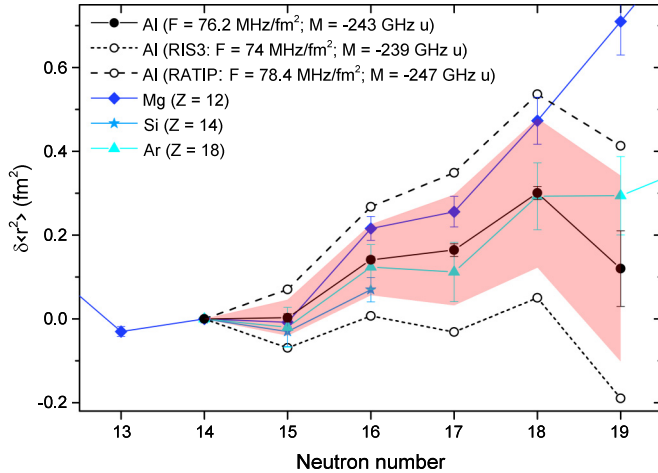
FIG. 3. Changes in mean-square charge radii of Al isotopes with respect to $N = 14$ obtained by combining the isotope shifts measured in this work with the atomic field and mass shift factors $F = 76.2$ MHz/fm^2 and $M = -243$ GHz u determined in Ref. [44], see text for details. The red shaded band indicates the systematic uncertainty due to a 1.5×10^{-4} relative uncertainty on the beam energy. Results using the F and M for the RIS3 and RATIP computational methods are separately indicated by the dotted and dashed lines, respectively. Data for neighboring isotopic chains are taken from [45–47]. The charge radii of Na ($Z = 11$) are not included in the plot because of the large systematic uncertainty on the slope [48].

a model-independent root mean-square radius $\sqrt{(\langle r^2 \rangle^{\mu e})}$, this Barrett equivalent radius was divided by the ratio of radial moments

$$V_2^e = \frac{R_{k\alpha}^e}{\sqrt{(\langle r^2 \rangle^e)}}$$

using the same values for α and k as in the muonic data. In the evaluation of both $R_{k\alpha}^e$ and $\langle r^2 \rangle^e$, the charge density distribution $\rho(r)$ measured in electron scattering experiments was used. Specifically, $\rho(r)$ determined from the Fourier-Bessel coefficients measured by Rothhaas and collaborators tabulated in Ref. [49] has been chosen since it has the benefit of being model-independent. Using this form of density distribution gave a value of $V_2^e = 1.2858(26)$. An accurate evaluation of the error on this value would require full knowledge of the uncertainty matrix associated with the calculation of these coefficients, which was unfortunately not available. Instead, the uncertainty was conservatively estimated by calculating the V_2^e values using model-dependent charge-density distributions determined with data from two different electron scattering experiments [50,51] yielding $V_2^e = 1.2847$ and $V_2^e = 1.2832$, respectively. The maximal difference between the V_2^e values computed from the three data sets gave the final error. Following this procedure, a root mean-square charge radius of $\sqrt{(\langle r^2 \rangle)} = 3.061(6)$ fm was obtained for ^{27}Al, corresponding to $\langle r^2 \rangle = 9.37(4)$ fm^2.

IV. $\delta \langle r^2 \rangle$ DEVELOPMENT TOWARDS $N = 20$

The mean-square charge radii relative to ^{27}Al are presented in Fig. 4. These charge radii show a normal odd-even staggering on top of a generally increasing trend between $N = 14$ and $N = 18$. At $N = 19$, however, the observed decrease in charge radius appears larger than expected from the odd-even staggering alone. Due to the relatively large uncertainty on the ^{32}Al value, the deviation from a normally increasing trend is only around 2σ. Nevertheless, it is interesting to discuss briefly what such a decrease might implicate if confirmed by a more precise measurement. Typically, a local dip in the trend of charge radii is seen in the vicinity of magic numbers, which is related to the reduced correlations at closed shells. It would therefore be natural to interpret the decline at $N = 19$ as the start of the dip leading up to the $N = 20$ shell closure. However, $N = 20$ is a peculiar case; such an effect is absent in the isotopic chains for which the charge radii are known so far. Above Al, the smoothly increasing charge radii of Ar, K, and Ca ($Z = 18$–20) across $N = 20$ have been interpreted as due to a balance between the monopole and the quadrupole proton-core polarization effects when neutrons fill the sd shell below $N = 20$ and the $f_{7/2}$ orbital above [47,52]. Below Al on the other hand, a sudden increase in charge radii seen for Na and Mg ($Z = 11$, 12) is explained by the onset of deformation in the island of inversion around $N = 20$ [45,53,54]. In this region, deformed intruder states in which neutrons are excited across $N = 20$ into the pf-shell become the ground state below the normally expected (spherical) sd states. The Al isotopes form the northern border of this island of inversion, with ^{33}Al at $N = 20$ being the transition point for which intruder configurations become significant [20,23]. Based on these observations, a dip at $N = 20$ in the Al charge radii trend would be quite unexpected. Hence, more precise measurements of the mean-square charge radii of ^{32}Al and beyond are needed to clarify this issue.

V. COMPARISON WITH VALENCE SPACE IN-MEDIUM SIMILARITY RENORMALIZATION GROUP RESULTS

We now compare the new measurements to calculations from the *ab initio* valence space in-medium similarity renormalization group method (VS-IMSRG) [5,6,8]. Since this method combines the broad applicability of the standard shell-model approach with microscopic interactions derived from two- and three-nucleon forces, it is an attractive option to study the structure of virtually all medium-mass isotopes, including open-shell isotopic chains like aluminum, in an *ab initio* framework.

A. Details of the calculations

In the VS-IMSRG a computationally tractable valence-space Hamiltonian is decoupled from the much larger Hilbert space via an approximately unitary transformation [4,55], and the resulting effective Hamiltonian is diagonalized using traditional shell-model codes. As outlined in Ref. [7], since the ensemble normal-ordering procedure captures $3N$ forces between valence nucleons, a specific Hamiltonian is produced for each isotope separately. Other operators, including
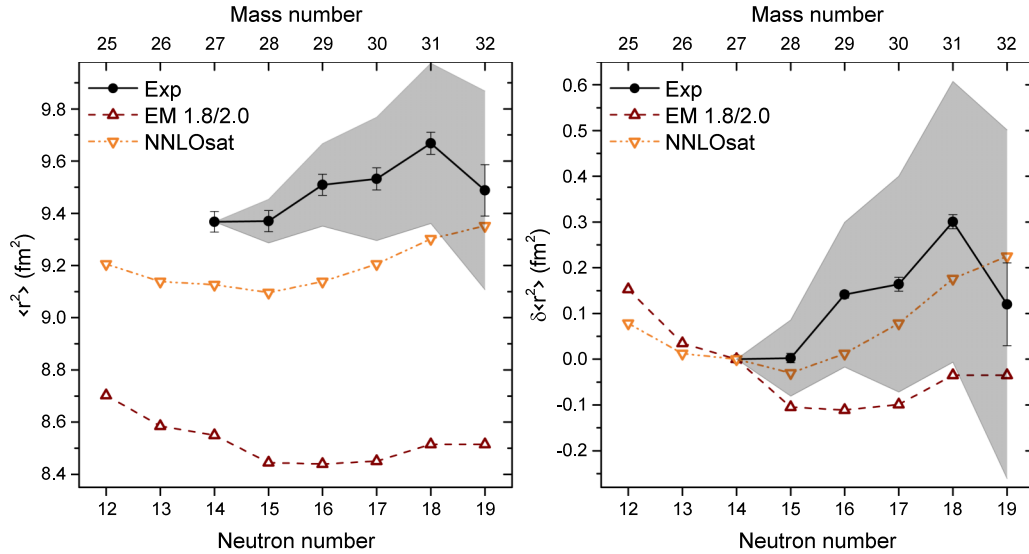
FIG. 4. Absolute mean-square charge radii $\langle r^2 \rangle$ and differences in mean-square charge radii $\delta \langle r^2 \rangle$ along the aluminum isotopic chain. Experimental results are compared with VS-IMSRG calculations. The gray band indicates the uncertainty on the slope of the charge radii arising due to the uncertainties on the atomic factors as well as the beam energy, as explained in Sec. III B.

those for charge radii and electromagnetic moments, can be treated consistently in the same framework [56,57]. Note that the $M1$ operator currently used does not include contributions from meson-exchange currents. While they are naively expected to result in some $M1$ quenching, these effects have so far only been implemented in light systems [58] and must be explicitly included to definitively determine their impact on the aluminium isotopes. In principle, all many-body physics is captured in the decoupling procedure since all the excitations outside of the valence space are renormalized into the valence-space Hamiltonian and consistent operators. In practice, however, truncation of all operators in the IMSRG expansion at the two-body level, the IM-SRG(2) approximation, is necessary to keep the problem computationally manageable. This means that higher-order terms induced when deriving the effective operator are not taken into account, which introduces some level of error in the procedure. Note that, unlike in typical shell-model calculations with empirically derived effective interactions, here bare charges and g factors are used.

In this work, the IMSRG calculations are performed in a harmonic oscillator basis with $\hbar\omega = 16$ MeV and quantum numbers $e = 2n + l \leqslant e_{\max} = 12$. A further cut off $e_1 + e_2 + e_3 \leqslant E_{3\max} = 16$ is applied for the $3N$ matrix elements. Using the new multishell variation of the VS-IMSRG [11], we are able to take ^{16}O as a core and the valence space that includes the sd proton orbitals and the $sdf_{7/2}p_{3/2}$ neutron orbitals. We also add the center-of-mass Hamiltonian to the initial Hamiltonian with the multiplier $\beta = 3$, as detailed in Ref. [11] to separate the center-of-mass motion. The final valence-space-diagonalizations are performed with the KSHELL shell-model code [59] and the effective operators were constructed using the IMSRG++ code [60].

We use two sets of $NN + 3N$ interactions derived from chiral effective field theory, EM 1.8/2.0 [56,61,62] and NNLO$_{\text{sat}}$ [63]. The EM 1.8/2.0 interaction is only constrained by data

of few-body systems ($A = 2, 3, 4$) and well reproduces binding energies to the $A = 100$ region [9,56], including proton and neutron driplines [12]. On the other hand, the NNLO$_{\text{sat}}$ interaction was optimized, including a selected set of binding energies and radii of carbon and oxygen isotopes ($A \leqslant 25$) on top of the standard few-body data. This has improved the simultaneous reproduction of charge radii and binding energies, also for isotopes much heavier than those used in the optimization [64–67].

B. Nuclear moments and charge radii

The calculated mean-square charge radii and nuclear moments together with our experimental results are shown in Figs. 4 and 5. In general, the observed trends are fairly well reproduced while the absolute scale deviates to varying extent, as discussed next. Note that, for the odd-odd isotopes, the state with the correct spin was not always calculated as the ground state but rather as an excited state below 850 keV. Although theoretical error bars are not yet available, this result is consistent with the 647 keV rms deviation found for VS-IMSRG calculations using the EM 1.8/2.0 interaction in the sd-shell [8]. In the following discussion and corresponding plots, only states with the correct spins are considered.

First, the absolute and differences in mean-square charge radii are shown in Fig. 4. Consistent with earlier findings [11,15,56], the absolute radii are very sensitive to the employed input interaction. As expected, the charge radii are underpredicted using the EM 1.8/2.0 interaction while the NNLO$_{\text{sat}}$ interaction generates radii in better, but not perfect, agreement with experiment. This is in keeping with previous studies which compare radii calculated via these interactions to those measured from experiment [15,56]. Moreover, the trend in $\delta \langle r^2 \rangle$ is different for both interactions. While the $\delta \langle r^2 \rangle$ obtained with EM 1.8/2.0 stay rather flat and do not reproduce the experimentally observed increasing trend, the slope of the NNLO$_{\text{sat}}$ is consistent within the present uncertainty on the
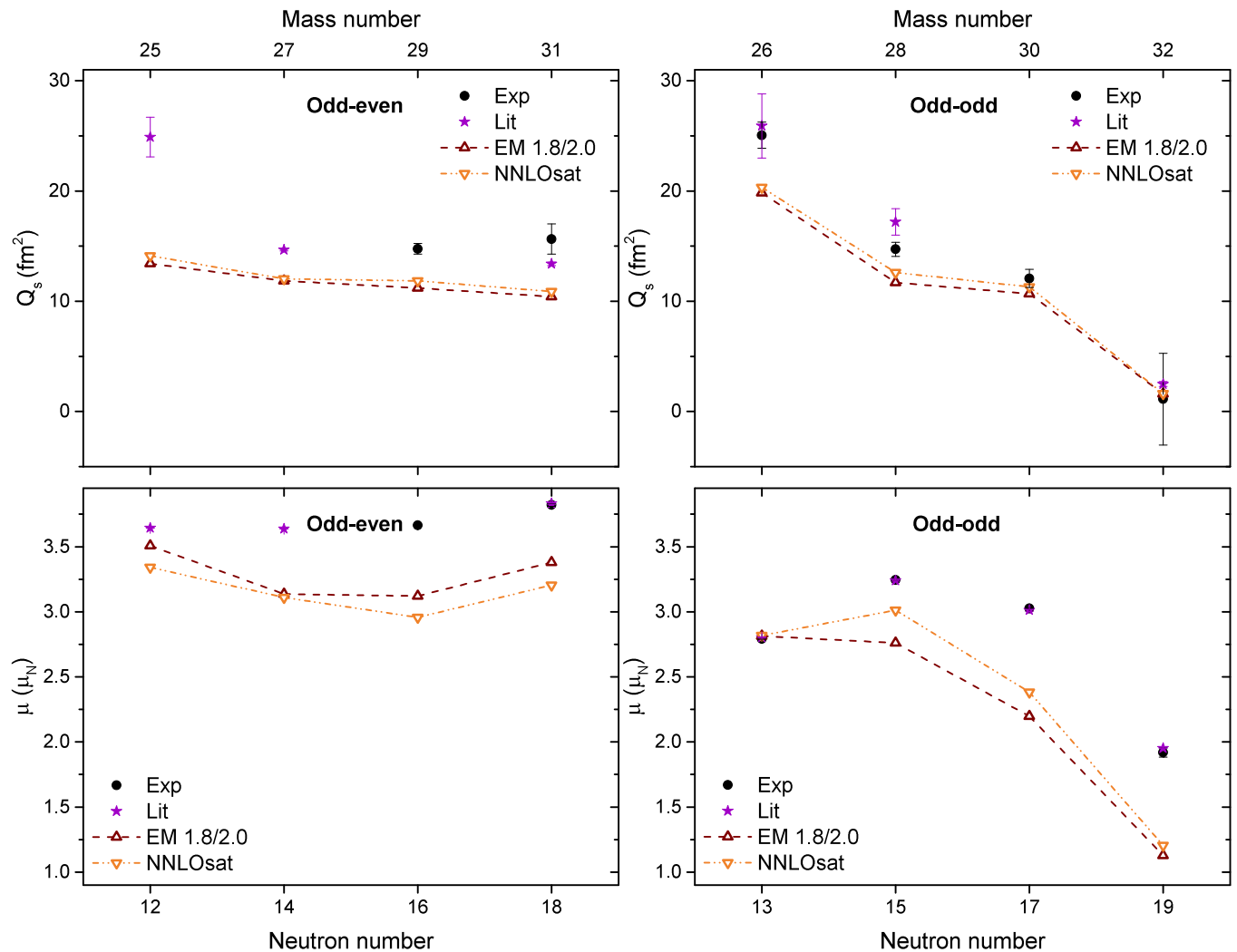
FIG. 5. Electric quadrupole moments (top) and magnetic dipole moments (bottom) of $^{27-32}$Al. Experimental values obtained in this work and found in the literature [39,40] are compared with calculations in the VS-IMSRG framework using the EM 1.8/2.0 and NNLO$_{sat}$ chiral interactions.

experimental slope. Nevertheless, in contrast with the experimental charge radii, neither interaction yields an appreciable odd-even staggering. Up to now, calculations of mean-square charge radii of open-shell nuclei with the VS-IMSRG method are limited to Cu ($Z = 29$) and Mn ($Z = 25$) [15,56] near the $Z = 28$ shell closure. In these cases, results using the EM 1.8/2.0 interaction (or other interactions of the same family like PWA 2.0/2.0) could well reproduce the observed experimental trends. It is therefore remarkable that the description of the Al isotopes seems to be more challenging. A systematic investigation of charge radii in the VS-IMSRG method should help to better understand this issue in the future.

Next, the quadrupole moments shown in the top row of Fig. 5 are examined. With the exception of ^{25}Al at $N = 12$,[1] the quadrupole moments are underestimated by

approximately 20% across the isotopic chain and both the EM 1.8/2.0 and NNLO$_{sat}$ interactions give nearly identical results. This underprediction is fully in line with earlier studies of $E2$-observables including static quadrupole moments and transition probabilities [$B(E2)$] [8,16,17,57], which identified the IMSRG(2) approximation as a major cause for the missing $E2$ strength. Due to the truncation of the operators at the two-body level, the effect of correlated multiparticle multihole pairs is underestimated. Furthermore, it was pointed out that the details of the input Hamiltonians do not have a large influence on the scale of the deviation. This conclusion is also supported here by the close similarity between the quadrupole moments obtained with both EM 1.8/2.0 and NNLO$_{sat}$ interactions.

Also for the magnetic moments in the bottom row of Fig. 5, both input interactions give comparable results which are in qualitative agreement with the experimental trend, while the absolute values are too small. So far, magnetic moments have only been studied intermittently in the VS-IMSRG approach [57,69] and investigations into the origin of the observed

---

[1]Note that a verification of the quadrupole moment of ^{25}Al, not remeasured in this work, would be advised due to the questionable quality of the obtained resonance in Ref. [68].

deviation is still work in progress. Since the meson-exchange currents show non-negligible effect on the magnetic moments in light nuclei [58], they will contribute at least partly to the discrepancy. Furthermore, it is reasonable to assume that the IMSRG(2) approximation will also affect the calculated magnetic moments, although different kinds of correlations might be important as compared with the quadrupole moment. Note that underestimated correlations could lead to magnetic moments which are either too small (like in this case) or too large (like, e.g., for ^{37,39}Ca [69,70]). This is similar to the effect of introducing effective g factors in phenomenological calculations. Despite an overall deviation, the good reproduction of the trend for both the magnetic and quadrupole moments suggests that few-nucleon effects in the model are correctly taken into account.

VI. SUMMARY

The $^{27-32}$Al isotopes were studied via high-resolution collinear laser spectroscopy at ISOLDE-CERN. State-of-the-art atomic physics calculations in combination with the isotope shifts measured in this work gave access to changes in mean-square charge radii of radioactive Al isotopes for the first time. An apparent reduction in the charge radius of ^{32}Al was discussed in the context of a potential shell effect at $N = 20$, although firm conclusions cannot be made due to its relatively large uncertainty. Furthermore, our measurements of the magnetic dipole moment of ^{29}Al and electric quadrupole moment of ^{29,30}Al fill the previously existing gap in nuclear moments near the valley of stability.

Experimental magnetic moments, quadrupole moments, and changes in mean-square charge radii of $^{25-32}$Al were compared with calculations within the VS-IMSRG approach using interactions derived from chiral effective field theory. No effective modifications to the g factor and charge were

introduced. Generally, the trends of the magnetic and quadrupole moments were well reproduced, while absolute values were underestimated. In this light, the large discrepancy between the published value of the quadrupole moment of ^{25}Al, not accessible in our current experiment, and the theoretical calculations warrants a remeasurement. The description of the mean-square charge radii proved to be more challenging, although calculations using the NNLO$_{sat}$ interaction are in agreement with the observed experimental slope. Because these observables are each sensitive to distinct features of the underlying nuclear structure, they are well-suited to provide complementary benchmarks for *ab initio* calculations.

[1] P. Campbell, I. Moore, and M. R. Pearson, Laser spectroscopy for nuclear structure physics, Prog. Part. Nucl. Phys. **86**, 127 (2015).

[2] E. Epelbaum, H.-W. Hammer, and U.-G. Meißner, Modern theory of nuclear forces, Rev. Mod. Phys. **81**, 1773 (2009).

[3] R. Machleidt and D. R. Entem, Chiral effective field theory and nuclear forces, Phys. Rep. **503**, 1 (2011).

[4] H. Hergert, S. K. Bogner, T. D. Morris, A. Schwenk, and K. Tsukiyama, The in-medium similarity renormalization group: A novel *ab initio* method for nuclei, Phys. Rep. **621**, 165 (2016).

[5] K. Tsukiyama, S. K. Bogner, and A. Schwenk, In-medium similarity renormalization group for open-shell nuclei, Phys. Rev. C **85**, 061304(R) (2012).

[6] S. K. Bogner, H. Hergert, J. D. Holt, A. Schwenk, S. Binder, A. Calci, J. Langhammer, and R. Roth, Nonperturbative Shell-Model Interactions from the In-Medium Similarity Renormalization Group, Phys. Rev. Lett. **113**, 142501 (2014).

[7] S. R. Stroberg, A. Calci, H. Hergert, J. D. Holt, S. K. Bogner, R. Roth, and A. Schwenk, Nucleus-Dependent Valence-Space

Approach to Nuclear Structure, Phys. Rev. Lett. **118**, 032502 (2017).

[8] S. Stroberg, S. Bogner, H. Hergert, and J. D. Holt, Nonempirical interactions for the nuclear shell model: An update, Annu. Rev. Nucl. Part. Sci. **69**, 307 (2019).

[9] T. D. Morris, J. Simonis, S. R. Stroberg, C. Stumpf, G. Hagen, J. D. Holt, G. R. Jansen, T. Papenbrock, R. Roth, and A. Schwenk, Structure of the Lightest Tin Isotopes, Phys. Rev. Lett. **120**, 152503 (2018).

[10] V. Manea *et al.*, First Glimpse of the $N = 82$ Shell Closure below $Z = 50$ from Masses of Neutron-Rich Cadmium Isotopes and Isomers, Phys. Rev. Lett. **124**, 092502 (2020).

[11] T. Miyagi, S. R. Stroberg, J. D. Holt, and N. Shimizu, *Ab initio* multi-shell valence-space Hamiltonians and the island of inversion, Phys. Rev. C **102**, 034320 (2020).

[12] S. R. Stroberg, J. D. Holt, A. Schwenk, and J. Simonis, *Ab Initio* Limits of Atomic Nuclei, Phys. Rev. Lett. **126**, 022501 (2021).

[13] R. Taniuchi *et al.*, ^{78}Ni revealed as a doubly magic stronghold against nuclear deformation, Nature (London) **569**, 53 (2019).

[14] P. Gysbers *et al.*, Discrepancy between experimental and theoretical β-decay rates resolved from first principles, Nat. Phys. **15**, 428 (2019).

[15] R. de Groote *et al.*, Measurement and microscopic description of odd-even staggering of charge radii of exotic copper isotopes, Nat. Phys. **16**, 620 (2020).

[16] J. Henderson *et al.*, Testing microscopically derived descriptions of nuclear collectivity: Coulomb excitation of ^{22}Mg, Phys. Lett. B **782**, 468 (2018).

[17] J. Henderson *et al.*, Coulomb excitation of the $|T_z| = \frac{1}{2}$, $A = 23$ mirror pair and systematics of ab-initio $E2$ strength, arXiv:2005.03796.

[18] T. Minamisono, Y. Nojiri, and S. Ochi, Measurement of the magnetic moment of the short-lived beta-emitter ^{28}Al polarized by means of the Overhauser effect in Li metal, Phys. Lett. B **106**, 38 (1981).

[19] A. C Morton *et al.*, Beta decay studies of nuclei near ^{32}Mg: Investigating the $\nu(f_{7/2})(d_{3/2})$ inversion at the $N = 20$ shell closure, Phys. Lett. B **544**, 274 (2002).

[20] P. Himpe *et al.*, g factors of ^{31,32,33}Al: Indication for intruder configurations in the ^{33}Al ground state, Phys. Lett. B **643**, 257 (2006).

[21] D. Kameda *et al.*, Measurement of the electric quadrupole moment of ^{32}Al, Phys. Lett. B **647**, 93 (2007).

[22] A. A. Kwiatkowski *et al.*, Observation of a crossover of S_{2n} in the island of inversion from precision mass spectrometry, Phys. Rev. C **92**, 061301(R) (2015).

[23] H. Heylen *et al.*, High-precision quadrupole moment reveals significant intruder component in $^{33}_{13}$Al$_{20}$ ground state, Phys. Rev. C **94**, 034312 (2016).

[24] Z. Y. Xu *et al.*, Nuclear moments of the low-lying isomeric 1^+ state of ^{34}Al: Investigation on the neutron 1p1h excitation across $N = 20$ in the island of inversion, Phys. Lett. B **782**, 619 (2018).

[25] R. Neugart, J. Billowes, M. L. Bissell, K. Blaum, B. Cheal, K. T. Flanagan, G. Neyens, W. Nörtershäuser, and D. T. Yordanov, Collinear laser spectroscopy at ISOLDE: New methods and highlights, J. Phys. G **44**, 064002 (2017).

[26] M. J. G. Borge and B. J. Jonson, Isolde past, present and future, J. Phys. G **44**, 044011 (2017); **44**, 079501 (2017).

[27] K. Kreim *et al.*, Nuclear charge radii of potassium isotopes beyond $N = 28$, Phys. Lett. B **731**, 97 (2014).

[28] U. Köster *et al.* (IS365, IS387, IS393, and ISOLDE Collaborations), On-line yields obtained with the ISOLDE RILIS, Nucl. Instrum. Methods Phys. Res., Sect. B **204**, 347 (2003).

[29] H. Fränberg *et al.*, Off-line commissioning of the ISOLDE cooler, Nucl. Instrum. Methods Phys. Res., Sect. B **266**, 4502 (2008).

[30] W. Gins, R. P. de Groote, M. L. Bissell, C. Granados Buitrago, R. Ferrer, K. M. Lynch, G. Neyens, and S. Sels, Analysis of counting data: Development of the SATLAS Python package, Comput. Phys. Commun. **222**, 286 (2018).

[31] N. Bendali, H. T. Duong, P. Juncar, J. M. Saint Jalm, and J. L. Vialle, Na$^+$-Na charge exchange processes studied by collinear laser spectroscopy, J. Phys. B: At. Mol. Phys. **19**, 233 (1986).

[32] A. Klose *et al.*, Tests of atomic charge-exchange cells for collinear laser spectroscopy, Nucl. Instrum. Methods Phys. Res., Sect. A **678**, 114 (2012).

[33] H. Lew, The hyperfine structure of the $^2P_{3/2}$ state of ^{27}Al: The nuclear electric quadrupole moment, Phys. Rev. **76**, 1086 (1949).

[34] K-H. Weber, J. Lawrenz, A. Obrebski, and K. Niemax, High-resolution laser spectroscopy of aluminium, gallium and thallium, Phys. Scr. **35**, 309 (1987).

[35] J. M. G. Levins, J. Billowes, P. Campbell, and M. R. Pearson, The quadrupole moment of Al, J. Phys. G **23**, 1145 (1997).

[36] J. Zhan-Kui, H. Lundberg, and S. Svanberg, Hyperfine structure of the $4s^2S_{1/2}$ state of ^{27}Al, Phys. Lett. A **92**, 27 (1982).

[37] A. Antusek and F. Holka, Absolute shielding scales for Al, Ga, and In and revised nuclear magnetic dipole moments of ^{27}Al, ^{69}Ga, ^{71}Ga, ^{113}In, and ^{115}In nuclei, J. Chem. Phys. **143**, 074301 (2015).

[38] V. Kellö, A. J. Sadlej, P. Pyykkö, D. Sundholm, and M. Tokman, Electric quadrupole moment of the ^{27}Al nucleus: Converging results from the AlF and AlCl molecules and the Al atom, Chem. Phys. Lett. **304**, 414 (1999).

[39] N. J. Stone, Table of recommended nuclear magnetic dipole moments, Tech. Rep. [INDC(NDS)-0794, 2019].

[40] M. De Rydt, M. Depuydt, and G. Neyens, Evaluation of the ground-state quadrupole moments of the (sd) nuclei, At. Data Nucl. Data Tables **99**, 391 (2013).

[41] A. M. Martensson-Pendrill, L. Pendrill, A. Salomonson, A. Ynnerman, and H. Warston, Reanalysis of the isotope shift and nuclear charge radii in radioactive potassium isotopes, J. Phys. B: At., Mol. Opt. Phys. **23**, 1749 (1990).

[42] B. Cheal, T. E. Cocolios, and S. Fritzsche, Laser spectroscopy of radioactive isotopes: Role and limitations of accurate isotope-shift calculations, Phys. Rev. A **86**, 042501 (2012).

[43] W. Nörtershäuser and C. Geppert, Nuclear charge radii of light elements and recent developments in collinear laser spectroscopy, in *The Euroschool on Exotic Beams*, edited by C. Scheidenberger and M. Pfützner (Springer, Berlin, Heidelberg, 2014), Vol. IV, pp. 233–292.

[44] L. Filippin, R. Beerwerth, J. Ekman, S. Fritzsche, M. Godefroid, and P. Jönsson, Multiconfiguration calculations of electronic isotope shift factors in Al I, Phys. Rev. A **94**, 062508 (2016).

[45] D. T. Yordanov *et al.*, Nuclear Charge Radii of $^{21-32}$Mg, Phys. Rev. Lett. **108**, 042504 (2012).

[46] I. Angeli and K. P. Marinova, Table of experimental nuclear ground state charge radii: An update, At. Data Nucl. Data Tables **99**, 69 (2013).

[47] K. Blaum, W. Geithner, J. Lassen, P. Lievens, K. Marinova, and R. Neugart, Nuclear moments and charge radii of argon isotopes between the neutron-shell closures $N = 20$ and $N = 28$, Nucl. Phys. A **799**, 30 (2008).

[48] G. Fricke and K. Heilig, *Nuclear Charge Radii* (Springer-Verlag, Berlin, Heidelberg, 2004).

[49] H. De Vries, C. W. De Jager, and C. De Vries, Nuclear charge-density-distribution parameters from elastic electron scattering, At. Data Nucl. Data Tables **36**, 495 (1987).

[50] R. M. Lombard and G. R. Bishop, The scattering of high-energy electrons by ^{27}Al, Nucl. Phys. A **101**, 601 (1967).

[51] G. Fey, H. Frank, W. Schütz, and H. Theissen, Nuclear Rms charge radii from relative electron scattering measurements at low energies, Eur. Phys. J. A **265**, 401 (1973).

[52] D. M. Rossi *et al.*, Charge radii of neutron-deficient ^{36}K and ^{37}K, Phys. Rev. C **92**, 014305 (2015).

[53] G. Huber *et al.*, Spins, magnetic moments, and isotope shifts of $^{21-31}$Na by high resolution laser spectroscopy of the atomic D_1 line, Phys. Rev. C **18**, 2342 (1978).

[54] F. Touchard *et al.*, Electric quadrupole moments and isotope shifts of radioactive sodium isotopes, Phys. Rev. C **25**, 2756 (1982).

[55] T. D. Morris, N. M. Parzuchowski, and S. K. Bogner, Magnus expansion and in-medium similarity renormalization group, Phys. Rev. C **92**, 034331 (2015).

[56] J. Simonis, S. R. Stroberg, K. Hebeler, J. D. Holt, and A. Schwenk, Saturation with chiral interactions and consequences for finite nuclei, Phys. Rev. C **96**, 014303 (2017).

[57] N. M. Parzuchowski, S. R. Stroberg, P. Navrátil, H. Hergert, and S. K. Bogner, Ab initio electromagnetic observables with the in-medium similarity renormalization group, Phys. Rev. C **96**, 034324 (2017).

[58] S. Pastore, S. C. Pieper, R. Schiavilla, and R. B. Wiringa, Quantum Monte Carlo calculations of electromagnetic moments and transitions in $A \leqslant 9$ nuclei with meson-exchange currents derived from chiral effective field theory, Phys. Rev. C **87**, 035503 (2013).

[59] N. Shimizu, T. Mizusaki, Y. Utsuno, and Y. Tsunoda, Thick-restart block Lanczos method for large-scale shell-model calculations, Comput. Phys. Commun. **244**, 372 (2019).

[60] S. R. Stroberg, https://github.com/ragnarstroberg/imsrg.

[61] K. Hebeler, S. K. Bogner, R. J. Furnstahl, A. Nogga, and A. Schwenk, Improved nuclear matter calculations from chiral low-momentum interactions, Phys. Rev. C **83**, 031301(R) (2011).

[62] J. Simonis, K. Hebeler, J. D. Holt, J. Menendez, and A. Schwenk, Exploring *sd*-shell nuclei from two- and three-nucleon interactions with realistic saturation properties, Phys. Rev. C **93**, 011302(R) (2016).

[63] A. Ekström, G. R. Jansen, K. A. Wendt, G. Hagen, T. Papenbrock, B. D. Carlsson, C. Forssén, M. Hjorth-Jensen, P. Navrátil, and W. Nazarewicz, Accurate nuclear radii and binding energies from a chiral interaction, Phys. Rev. C **91**, 051301(R) (2015).

[64] R. F. Garcia Ruiz *et al.*, Unexpectedly large charge radii of neutron-rich calcium isotopes, Nat. Phys. **12**, 594 (2016).

[65] V. Lapoux, V. Somà, C. Barbieri, H. Hergert, J. D. Holt, and S. R. Stroberg, Radii and Binding Energies in Oxygen Isotopes: A Challenge for Nuclear Forces, Phys. Rev. Lett. **117**, 052501 (2016).

[66] G. Hagen, Neutron and weak-charge distributions of the ^{48}Ca nucleus, Nat. Phys. **12**, 186 (2015).

[67] S. Kaufmann *et al.*, Charge Radius of the Short-Lived ^{68}Ni and Correlation with the Dipole Polarizability, Phys. Rev. Lett. **124**, 132502 (2020).

[68] K. Matsuta *et al.*, Hyperfine interaction of 25Al in α-Al$_2$O$_3$ and its quadrupole moment, in *HFI/NQI 2007*, edited by A. Pasquevich, M. Rentería, E. Baggio Saitovitch, and H. Petrilli (Springer, Berlin, Heidelberg, 2008), pp. 495–499.

[69] A. Klose *et al.*, Ground-state electromagnetic moments of ^{37}Ca, Phys. Rev. C **99**, 061301(R) (2019).

[70] R. F. Garcia Ruiz *et al.*, Ground-state electromagnetic moments of calcium isotopes, Phys. Rev. C **91**, 041304(R) (2015).